nature portfolio

https://doi.org/10.1038/s41560-022-00985-z

Supplementary information

Understanding what limits the voltage of polycrystalline CdSeTe solar cells

In the format provided by the authors and unedited

Supplementary Information

Understanding what limits the voltage of polycrystalline CdSeTe solar cells

Arthur Onno,[1]* Carey Reich,[2] Siming Li,[3] Adam Danielson,[2] William Weigand,[1] Alexandra Bothwell,[3] Sachit Grover,[4] Jeff Bailey,[4] Gang Xiong,[4] Darius Kuciauskas,[3] Walajabad Sampath,[2] and Zachary C. Holman[1]*

[1]*School of Electrical, Computer and Energy Engineering, Arizona State University, Tempe, AZ, 85287, United States*

[2]*Department of Mechanical Engineering, Colorado State University, Fort Collins, CO 80523, United States*

[3]*National Renewable Energy Laboratory, Golden, CO 80401, USA*

[4]*California Technology Center, First Solar Inc., Santa Clara, CA 95050, USA*

***Corresponding authors:** Arthur Onno (arthur.onno@asu.edu), Zachary C. Holman (zachary.holman@asu.edu)

Supplementary Discussion 1 — Theory: Calculation of the thermodynamic voltage limit $V_{oc,ideal}$

As first described by Ross and later fully detailed by Würfel,[1,2] Planck's law of radiative emission can be generalized to two-level photochemical systems—in particular, semiconductor photovoltaic absorbers—by considering the chemical potential of emitted photons. In the case of a semiconductor photovoltaic absorber, the emitted photons are in equilibrium with the recombining electron-hole pairs and, consequently, the chemical potential of photons matches the difference of electrochemical potential (*i.e.*, the quasi-Fermi-level splitting $QFLS = q \times iV$) between the electrons and the holes—that is, band-to-band recombination between carriers in equilibrium within the conduction and valence bands is lossless and reversible. The spectrally resolved emitted photon current $\phi_{lum}(\lambda)$ is then given by:[2]

$$\phi_{lum}(\lambda) = a(\lambda)\frac{2\pi c}{\lambda^4}\frac{1}{exp\left(\frac{\frac{hc}{\lambda} - q \times iV}{k_B T}\right) - 1}, \tag{S1}$$

with λ the wavelength, $a(\lambda)$ the spectrally resolved absorptance of the sample, c the speed of light in vacuum, h the Planck constant, k_B the Boltzmann constant, and T the temperature of the sample.

In photovoltaic absorbers operating under normal conditions (1-sun excitation or below), $hc/\lambda \gg q \times iV$ in the region of the spectrum where $a(\lambda) > 0$ (in the vicinity and above the bandgap of the material). As a result, the Boltzmann approximation can be used—the -1 in the denominator in Equation (S1) can be ignored—yielding:

$$\phi_{lum}(\lambda) = a(\lambda)\frac{2\pi c}{\lambda^4 exp\left(\frac{hc}{\lambda k_B T}\right)} exp\left(\frac{q \times iV}{k_B T}\right) = a(\lambda)\phi_{BB}(\lambda, T) exp\left(\frac{q \times iV}{k_B T}\right). \tag{S2}$$

Here $\phi_{BB}(\lambda, T)$ is the blackbody photon current at temperature T, given by:

$$\phi_{BB}(\lambda, T) = \frac{2\pi c}{\lambda^4 \exp\left(\frac{hc}{\lambda k_B T}\right)}. \tag{S3}$$

Considering that the thermal equilibrium is broken by an excitation photon current $\phi_{exc}(\lambda)$, the total absorbed photon current—including the black body photon current absorbed from the surroundings of the sample at temperature T—is given by:

$$\phi_{abs}(\lambda) = a(\lambda)[\phi_{exc}(\lambda) + \phi_{BB}(\lambda, T)]. \tag{S4}$$

The total (integrated) emitted photon current $\Phi_{lum} = \int \phi_{lum}(\lambda)d\lambda$ can then be compared to the total absorbed photon current $\Phi_{abs} = \int \phi_{abs}(\lambda)d\lambda$. In the best-case scenario, detailed balance between absorption and emission ($\Phi_{lum} = \Phi_{abs}$) with no non-radiative recombination and no charge extraction (open circuit) dictates the upper limit $V_{oc,ideal}$ of the internal voltage *iV*:

$$\int \phi_{lum}(\lambda)d\lambda = \int \phi_{abs}(\lambda)d\lambda, \tag{S5a}$$

$$\int a(\lambda)\phi_{BB}(\lambda, T)exp\left(\frac{q \times V_{oc,ideal}}{k_B T}\right)d\lambda = \int a(\lambda)[\phi_{exc}(\lambda) + \phi_{BB}(\lambda, T)]d\lambda, \tag{S5b}$$

$$exp\left(\frac{q \times V_{oc,ideal}}{k_B T}\right) = \frac{\int a(\lambda)[\phi_{exc}(\lambda) + \phi_{BB}(\lambda, T)]d\lambda}{\int a(\lambda)\phi_{BB}(\lambda, T)d\lambda}, \tag{S5c}$$

$$V_{oc,ideal} = \frac{k_B T}{q} \ln\left(\frac{\int a(\lambda)\phi_{exc}(\lambda)d\lambda}{\int a(\lambda)\phi_{BB}(\lambda, T)d\lambda} + 1\right). \tag{S5d}$$

It is important to note that, from Equation (S5d), $V_{oc,ideal}$ depends solely on the absorptance of the sample, the illumination, and the sample temperature. Thus, under standard test conditions ($\phi_{exc}(\lambda)$ corresponds to AM1.5G illumination, T=298.15 K), knowledge of the absorptance of the sample $a(\lambda)$ is sufficient to determine its $V_{oc,ideal}$. Equation (S5d) can be rewritten in terms of equivalent charge current densities, yielding a more familiar “diode-like” expression:

$$V_{oc,ideal} = \frac{k_B T}{q} \ln\left(\frac{J_{ph}}{J_{0,rad}} + 1\right) \cong \frac{k_B T}{q} \ln\left(\frac{J_{sc}}{J_{0,rad}} + 1\right), \quad \text{(S5e)}$$

with $J_{ph} = q \times \int a(\lambda)\phi_{exc}(\lambda)d\lambda$ and $J_{0,rad} = q \times \int a(\lambda)\phi_{BB}(\lambda)d\lambda$. Under reasonable assumptions J_{ph} is equal to the short-circuit current density J_{sc}.

Furthermore, as the term in the exponent in Equation (S2) is independent of wavelength, the shapes of the absorption and emission spectra, $a(\lambda)$ and $\phi_{lum}(\lambda)$, can be determined from one another provided that the temperature—and, thus, the blackbody photon current $\phi_{BB}(\lambda)$—is known.[1-4] This is illustrated in Supplementary Figure 1 for a representative CdSeTe solar cell: multiplying the cell's absorptance, approximated as its normalized external quantum efficiency (EQE), by the blackbody photon current at room temperature results in a spectrum that matches the emission spectrum obtained from photoluminescence (PL) corrected for temperature. Thus, in practice, $V_{oc,ideal}$ can be determined from either an EQE measurement or a PL measurement (in place of a true absorptance measurement), and both measurements can be combined to improve the accuracy of the calculation. In this contribution, we use both approaches, depending on whether we are examining uncontacted test structures (*e.g.*, double heterostructures)—for which the EQE cannot be measured—or finished devices.

The shaded area under the curve in Supplementary Figure 1a corresponds to the denominator $\int a(\lambda)\phi_{BB}(\lambda, T)d\lambda$ in Equation (S5d). As, in the wavelength region where common photovoltaic absorbers have their bandgaps (400–2000 nm), the room-temperature blackbody photon current increases quasi-exponentially with wavelength (Equation (S3)) whereas the variation of the solar photon current is comparatively negligible (see Supplementary Figure 1b and note that this term is in the numerator of Equation (S5d)), any sub-bandgap absorption will reduce $V_{oc,ideal}$. In the exemplary case of a Cu-doped CdSeTe solar cell shown in Supplementary Figure

1, as the absorptance (approximated by the EQE) decreases sub-exponentially below the bandgap, a second peak arises, approximately doubling the total absorbed blackbody photon current. Conversely, the absorbed solar photon current $\int a(\lambda)\phi_{AM1.5G}(\lambda)d\lambda$ in the numerator increases marginally. As a result, $V_{oc,ideal}$ decreases by 15–20 mV, even though this sub-bandgap behavior is imperceptible from the EQE spectrum on a linear scale (Supplementary Figure 1c). Thus, sub-bandgap features are detrimental and should be avoided, as they lower the "effective bandgap" of the device and reduce its achievable voltage $V_{oc,ideal}$ without substantial gains in photocurrent.

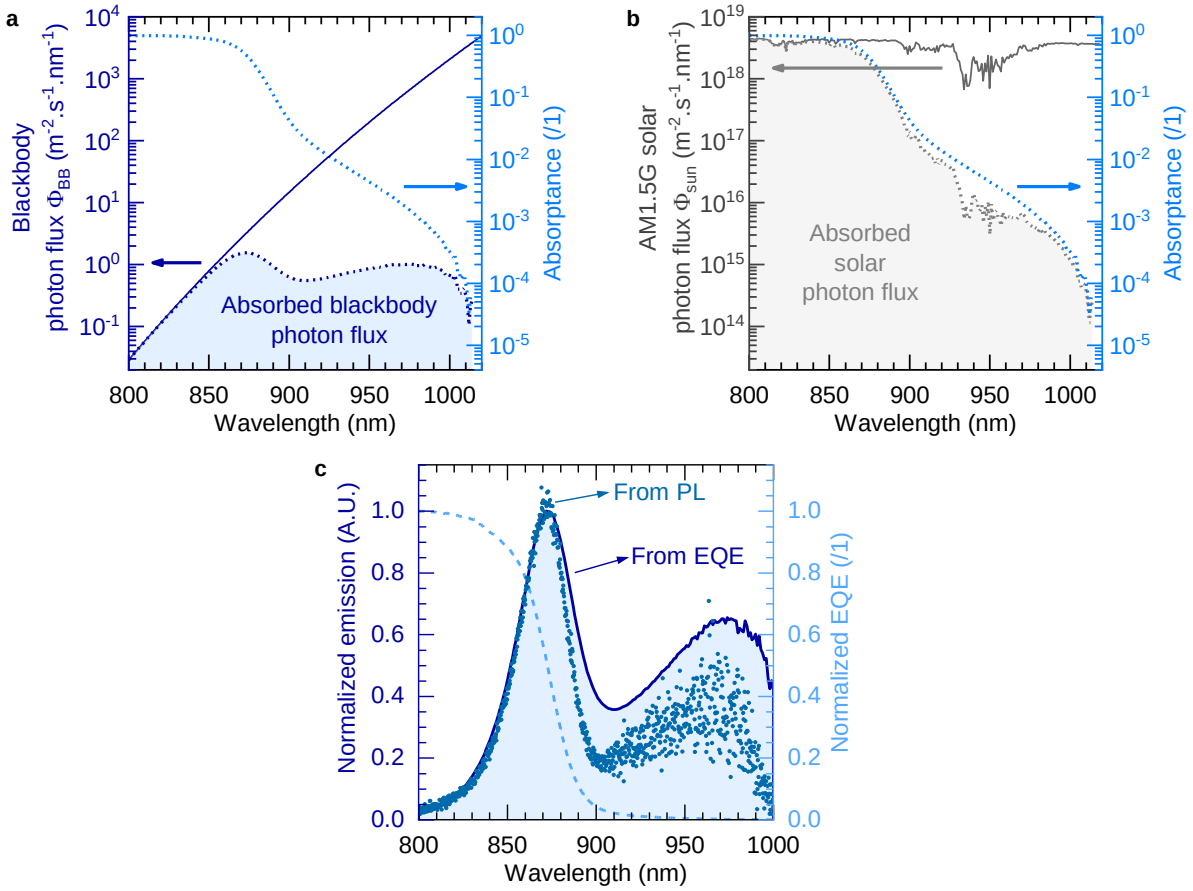

Supplementary Figure 1. Using the reciprocity between absorption and emission in the dark to calculate $V_{oc,ideal}$. a) Illustration, in the case of a representative Cu-doped CdSeTe solar cell, of the calculation of the absorbed blackbody photon current (at room temperature) from the normalized EQE, yielding the emission spectrum. Althought the log scales cover different ranges, they vary by the same number of orders of magnitude. **b)** Illustration, for the same solar cell, of the calculation of the absorbed AM1.5G photon current from the normalized EQE, yielding the photogenerated current. Again, the log scales vary by the same number of orders of magnitude. **c)** Comparison between normalized emission spectra at room temperature from the same representative CdSeTe device, obtained from PL measurement and from multiplying the EQE by the blackbody photon current. The PL data are corrected for temperature (see Supplementary Methods 1 for details). The normalized EQE is shown for reference.

Supplementary Discussion 2 — Theory: the role of non-radiative recombination, from $V_{oc,ideal}$ to iV_{oc}

When taking non-reversible processes—such as non-radiative recombination, loss of photons through parasitic absorption, and escape through the rear side of the absorber—into account, the total luminescent photon current $\Phi_{lum} = \int \phi_{lum}(\lambda)d\lambda$ emitted from the front surface of the sample is a fraction of the absorbed photon current $\Phi_{abs} = \int a(\lambda)\phi_{AM1.5G}(\lambda)d\lambda$. The *ERE* is then defined as the ratio between the emitted and absorbed integrated photons currents:

$$ERE = \frac{\Phi_{lum}}{\Phi_{abs}} = \frac{\int \phi_{lum}(\lambda)d\lambda}{\int \phi_{abs}(\lambda)d\lambda} = exp\left(\frac{q \times iV_{oc}}{k_B T}\right)\frac{\int a(\lambda)\phi_{BB}(\lambda,T)d\lambda}{\int a(\lambda)[\phi_{exc}(\lambda) + \phi_{BB}(\lambda,T)]d\lambda}. \quad \text{(S6a)}$$

Equation (S6a) can then be reorganized to yield the Ross' relationship between iV_{oc}, $V_{oc,ideal}$, and *ERE*:[1]

$$\frac{k_B T}{q}\ln(ERE) = iV_{oc} + \frac{k_B T}{q}\ln\left(\frac{\int a(\lambda)\phi_{BB}(\lambda,T)d\lambda}{\int a(\lambda)[\phi_{exc}(\lambda) + \phi_{BB}(\lambda,T)]d\lambda}\right), \quad \text{(S6b)}$$

$$iV_{oc} = V_{oc,ideal} - \frac{k_B T}{q}|\ln(ERE)|. \quad \text{(S6c)}$$

Note that the entire derivation presented here refers to the absorption and emission of a slab of semiconductor from and toward a half-hemisphere. We thus assume that the sample or device under study is flat and mono-facial (as opposed to bi-facial) and the *ERE* we consider corresponds to the emitted photons escaping from the front of the sample. As demonstrated by Ganapati *et al*.,[5] in this convention, the maximal achievable *ERE* is not necessarily 1, depending on the optics of the sample. For example, a symmetric sample with a semiconductor/air interface at the front and at the back will have a maximum *ERE* of 0.5 as emitted photons will have an equal chance of escaping the absorber through the front or the back surfaces. We choose this convention

because of the *ERE* measurement setup we use, which only accounts for photons emitted from the front of the sample.

Supplementary Discussion 3 — Theory: the role of selectivity, from iV_{oc} to V_{oc}

For the external open-circuit voltage V_{oc} to approach the internal open-circuit voltage iV_{oc}, voltage losses due to carrier transport must be minimized. As detailed by Würfel *et al*. and later expanded by Onno *et al*., separation and transport of charge carriers is dictated by the partial resistances experienced by electrons and holes.[6,7] Electrons (holes, respectively) follow the gradient of their quasi-Fermi level (QFL) and, locally, the resulting electron (hole) partial current is the product of the QFL gradient by the partial resistivity to electrons (holes). This is still true at open circuit: even though there is no net charge current flowing in or out of the device, the partial currents of electrons and hole in the absorber are not zero, they just match at every position in the device, leading to a recombination current at each electrode.

Integrating from the maximum of the QFL splitting to its collapse at the interfaces with the electrode, Onno *et al*. have shown that the problem can be reduced by considering the combined partial resistances ρ_e and ρ_h experienced by electrons and holes through the absorber and the contact layers up to the electrode interfaces. These partial resistances—which are injection-dependent—are defined from the maximum of the QFL splitting towards both the front and the back of the device (*i.e*., we need to consider four partial resistances: ρ_e^{front}, ρ_h^{front}, ρ_e^{back}, and ρ_h^{back}). Note that the contribution of each region of the absorber to these partial resistances is weighted by the generation profile to account for the difference in the resistance experienced by carriers generated closer to or farther from the interface with the electrode.[7] Ideally, the partial resistances to electrons and holes are negligible in the absorber and the combined partial resistances are dominated by the contributions from the contact layers.

At open circuit, the recombination current at each electrode is a decreasing function of the *sum* $\rho_e + \rho_h$ of the partial resistances toward that electrode. That is, to minimize recombination at the electrode, the resistance to *at least one type* of charge carriers must be high (*i.e.*, the contact layer must be blocking at least one type of charge carriers to be passivating). Thus, iV_{oc} increases with the sums $\rho_e^{front} + \rho_h^{front}$ and $\rho_e^{back} + \rho_h^{back}$ and, if iV_{oc} is high, at least one of the resistances toward each interface is high.

On the other hand, voltage losses due to carrier transport are governed by the selectivity of the device. In our case, the selectivity of the front electron contact is defined as:

$$S_{oc,e}^{front} = 1 - \frac{\rho_e^{front}}{\rho_e^{front} + \rho_h^{front}} < 1, \tag{S7a}$$

the selectivity the back hole contact is defined as:

$$S_{oc,h}^{back} = 1 - \frac{\rho_h^{back}}{\rho_e^{back} + \rho_h^{back}} < 1 \tag{S7b}$$

and the total selectivity of the device is then given by:

$$S_{oc} = S_{oc,e}^{front} + S_{oc,h}^{back} - 1 < 1. \tag{S7c}$$

V_{oc} is then directly related to iV_{oc} through:[7]

$$V_{oc} = S_{oc} \times iV_{oc} \tag{S8}$$

$S_{oc} = V_{oc}/iV_{oc}$ is, thus, a *measurable* metric of the selectivity of the device. For V_{oc} to approach iV_{oc}, high *ratios* are needed between the partial resistances to carriers to be extracted (electrons at the front, holes at the back) and to carriers to be blocked (holes at the front, electrons at the back). In particular, if $0.1 \times iV_{oc} < V_{oc} < 0.9 \times iV_{oc}$, the partial resistances to electrons and holes are of the same order of magnitude toward at least one of the electrodes.

Finally, to ensure minimal resistance losses when a net current flows out of the cell and, thus, to achieve a high fill factor, the conductivities to the carriers to be extracted (electrons at the front, holes at the back) must be both high in absolute value, with the associated partial resistances being consequently small. From Equations S7 and S8, it stems that a poor selectivity is due to either a poor passivation—the sum of the partial resistances is too small—or a poor conductivity —the partial resistances to the carriers to be extracted are too high.

Supplementary Discussion 4 — The full picture: parsing voltage losses

The complete voltage loss analysis is illustrated schematically in Supplementary Figure 2a in the case of a highly doped absorber. Selectivity losses ($iV_{oc} - V_{oc}$) are generally overlooked by the CdTe community, and the internal and external voltages iV_{oc} and V_{oc} are often confused, with the underlying (but typically wrong) assumption that the contacts are perfectly selective and that, consequently, the iV_{oc} is fully extracted. As shown in Supplementary Figures 2b and 2c, V_{oc} alone does not tell the full story: two devices can have the exact same V_{oc} for different reasons and be limited by selectivity (Supplementary Figure 2b), non-radiative recombination (Supplementary Figure 2c), or a combination of both. As shown in Supplementary Figure 2d, in the extreme case of a symmetric structure, iV_{oc} can be high and the sample can exhibit a strong luminescence—as is the case with double heterostructures—even though the sample has no selectivity and V_{oc} is equal to zero.

Supplementary Figure 2a shows the particular case of a highly doped p-type sample ($N_A \gg 10^{16}$ cm^{-3} for CdSeTe). The quasi-Fermi level of holes is then set by the acceptor concentration, even under 1-sun illumination with no non-radiative recombination. That is, the iV_{oc} only depends on the quasi-Fermi level—and, thus, on the concentration—of electrons. In detail, under uniform excess generation rate ΔG, the electron concentration n_e is approximately equal to the excess carrier concentration Δn:

$$n_e = \frac{n_i^2}{N_A} + \Delta n \cong \Delta n = \Delta G \tau \tag{S9a}$$

$$\text{Highly doped case: } n_h = N_A + \Delta n \cong N_A \tag{S9b}$$

with n_i the intrinsic carrier concentration, τ the minority-carrier lifetime, and n_h the hole concentration. As shown in Supplementary Figure 2a, iV_{oc} is then given by:

$$\text{Highly doped case: } iV_{oc} = \frac{k_B T}{q} \ln\left(\frac{n_h n_e}{n_i^2}\right) \cong \frac{k_B T}{q} \ln\left(\frac{\Delta G N_A \tau}{n_i^2}\right). \quad \text{(S10)}$$

However, in intrinsic or low-doped samples ($N_A \ll 10^{15}$ cm^{-3} in the case of CdSeTe), the acceptor concentration is lower than the excess carrier concentration even under moderate injection ($N_A \ll \Delta n$). Thus, as shown in Supplementary Figure 3, the concentrations and the quasi-Fermi levels of both electrons and holes are set by the excess carrier concentration and *together* they set iV_{oc}:

$$n_e = \frac{n_i^2}{N_A} + \Delta n \cong \Delta n = \Delta G \tau, \quad \text{(S11a)}$$

$$\text{Low-doped case: } n_h = N_A + \Delta n \cong \Delta n = \Delta G \tau, \quad \text{(S11b)}$$

$$\text{Low-doped case: } iV_{oc} = \frac{k_B T}{q} \ln\left(\frac{n_h n_e}{n_i^2}\right) \cong \frac{2k_B T}{q} \ln\left(\frac{\Delta G \tau}{n_i}\right) \quad \text{(S12)}$$

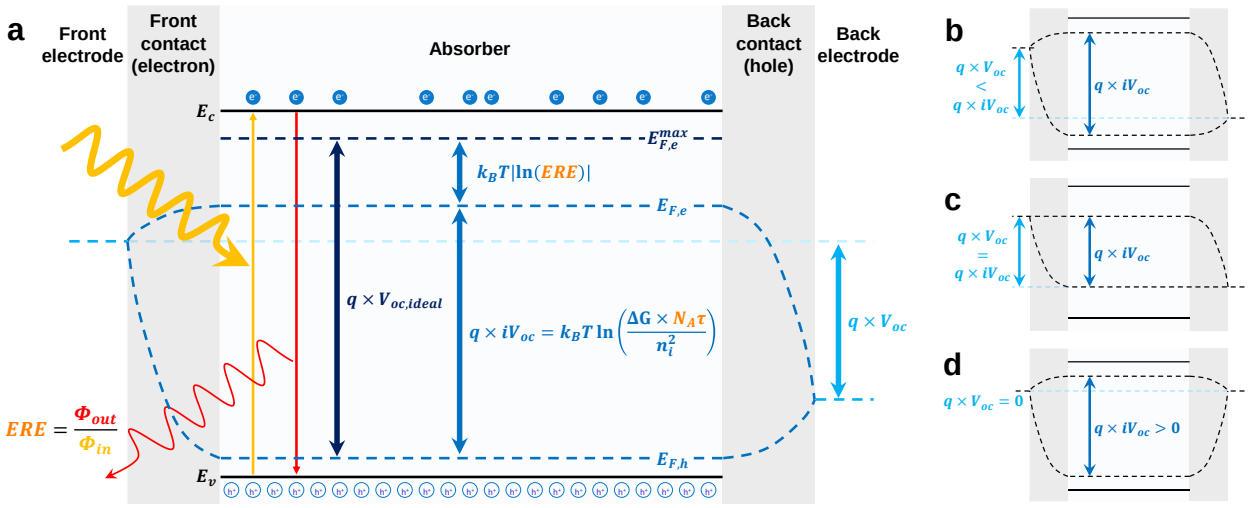

Supplementary Figure 2. Parsing voltage losses in the case of a highly doped absorber. a) Schematic breakdown of voltage losses in solar cells, from $V_{oc,ideal}$ to iV_{oc} to V_{oc}. The band structures of the contacts and of the electrodes are not represented for the sake of generality. For simplicity, a highly doped p-type absorber ($\gg 10^{16}$ cm^{-3} for CdSeTe) is shown here so that the quasi-Fermi level of holes is fixed by the acceptor concentration N_A independent of the injection level. **b)** Case of a cell with excellent surface passivation and bulk material quality that is limited by the selectivity of its contacts. **c)** Case of a cell with excellent selectivity that is limited by non-radiative recombination. **d)** Case of a symmetric double heterostructure with a high iV_{oc} but no external voltage.

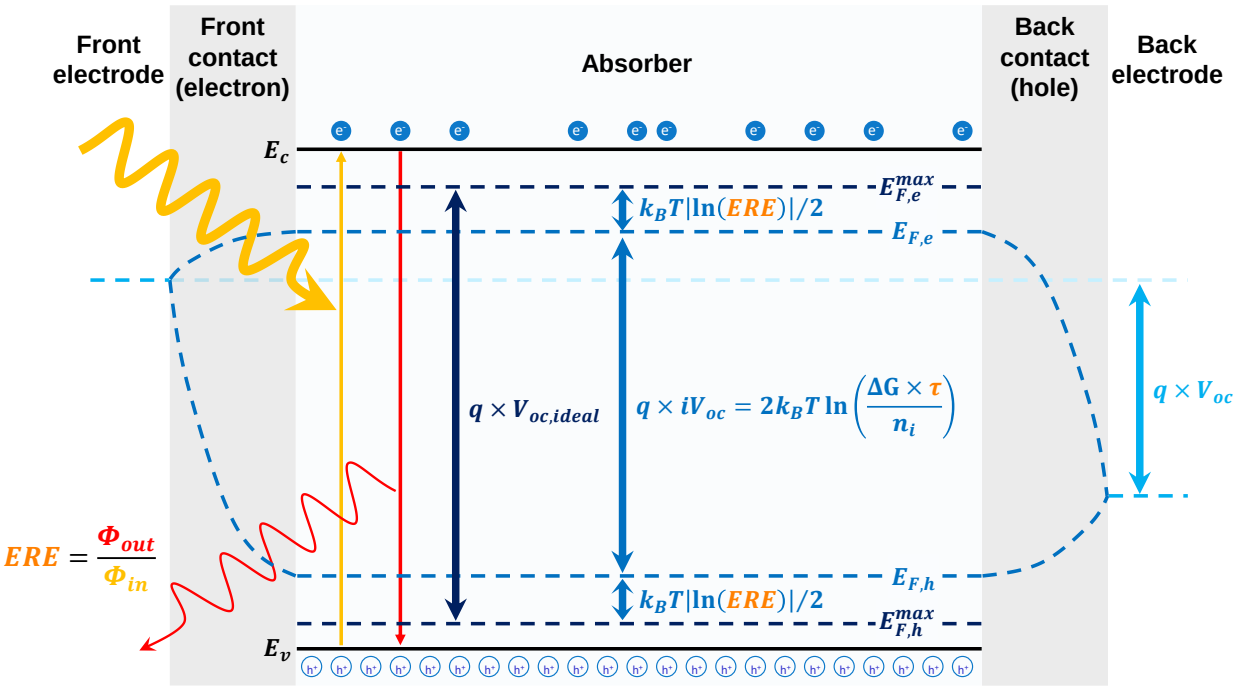

Supplementary Figure 3. Parsing voltage losses in solar cells in the case of a low-doped or intrinsic absorber. iV_{oc} now only depends on the excess carrier lifetime τ, as the concentrations and, thus, the quasi-Fermi levels of both electrons and holes are set by the excess carrier concentration.

Supplementary Methods 1 — Temperature correction of photoluminescence spectra to calculate $V_{oc,ideal}$

From Equation (S2), the spectrally resolved luminescent photon current is proportional to the product of the absorptance and the blackbody photon current at the sample temperature. Provided that the PL system used is spectrally calibrated, the PL signal $S_{PL}(\lambda)$ will have the same proportionality (even if it is not calibrated in absolute photon numbers):

$$S_{PL}(\lambda) \propto a(\lambda)\phi_{BB}(\lambda, T). \quad \text{(S13)}$$

Given that $a(\lambda)$ is approximately constant and equal to 1 at short wavelengths (above the bandgap), the temperature of the sample can be determined by fitting the (scaled) blackbody photon current to the PL signal using temperature as the only free parameter. This is shown in Supplementary Figure 4, where the best fit is obtained at a sample temperature of 323 K, which is physically consistent with the measurement. Similarly, the temperatures used for the correction of the PL spectra from First Solar samples, shown in Supplementary Table 3, fall within a physically reasonable range.

The absorptance of the sample can then be determined by dividing the PL signal by the blackbody photon current and scaling to $a(\lambda) = 1$ above the bandgap (at 840 nm in the case shown here). At this stage, the fit can be checked by ensuring that the absorptance plateaus above bandgap, as shown in Supplementary Figure 5a. A too low fitting temperature will lead to a sloped calculated absorptance with no plateau, a too high fitting temperature will lead to a dip in the absorptance above bandgap, as shown in Supplementary Figure 5b.

Using the absorptance determined from PL, the emission spectrum under standard test conditions (T=298.15 K) can be reconstructed, as shown in Supplementary Figure 6, and $V_{oc,ideal}$

can be calculated. In the case shown in Supplementary Figures 4–6, we find $V_{oc,ideal}$=1131.2 mV, with a loss of approximately 10 mV due to sub-bandgap features. As the sample temperature is typically above 298.15 K during PL measurements, this temperature correction usually increases the contribution from sub-bandgap features, which become less visible at higher temperature. The sensitivity of this method to calculate $V_{oc,ideal}$ is shown in Supplementary Table 1. Errors of up to 35–40 K, which yield non-physical absorptance (as shown in Supplementary Figure 5b), only lead to an error in $V_{oc,ideal}$ of approximately 10 mV. The error is less than 5 mV when the error in the assumption of the temperature is below 20 K.

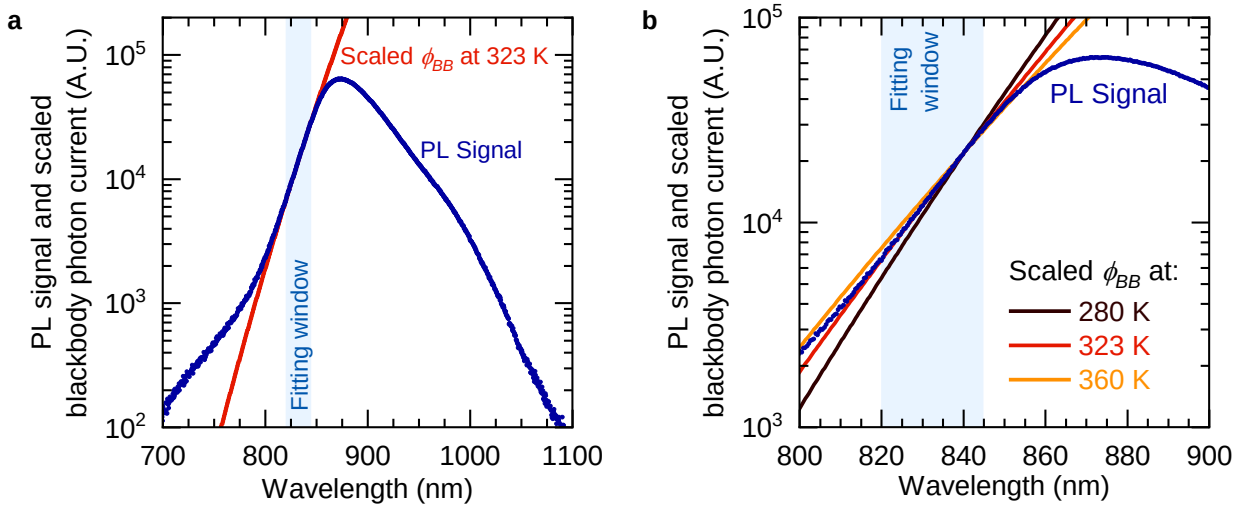

Supplementary Figure 4. Determination of the sample temperature during PL measurement of a CdSeTe sample by fitting the PL signal at short wavelenghts to the scaled blackbody photon current ϕ_{BB}. a) Illustration of the technique, with the blackbody photon current scaled to match the PL signal at 840 nm. The fitting window is 820–845 nm. **b)** Zoom on the fitting region, with blackbody photon currents at higher and lower temperatures (again, scaled to match the PL signal at 840 nm) showing the uniqueness of the fit.

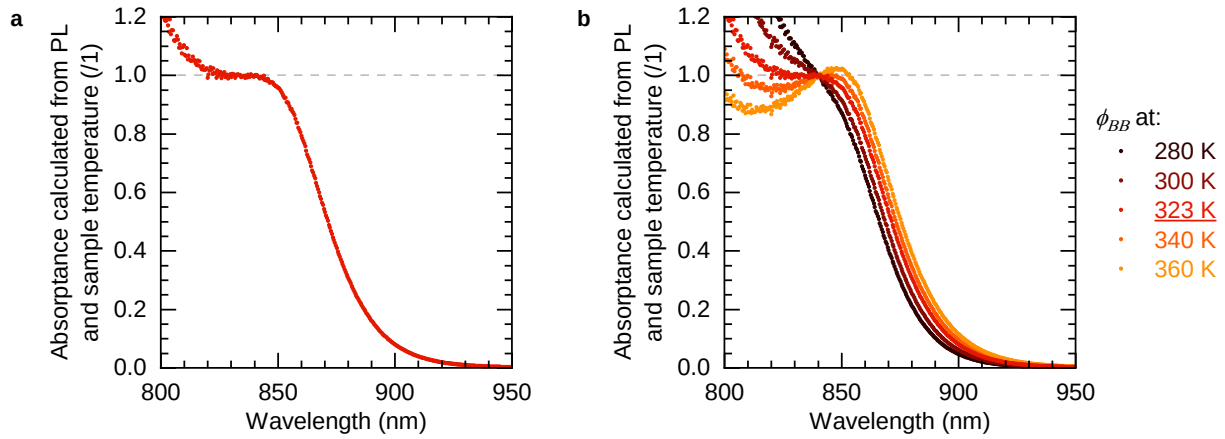

Supplementary Figure 5. Determination of the absorptance of a CdSeTe sample by dividing the PL signal by the blackbody photon current ϕ_{BB} at the sample temperature a) Absorptance obtained with ϕ_{BB} at T=323 K. **b)** Absorptances obtained with higher and lower assumptions on the temperature, demonstrating the uniqueness of the fit.

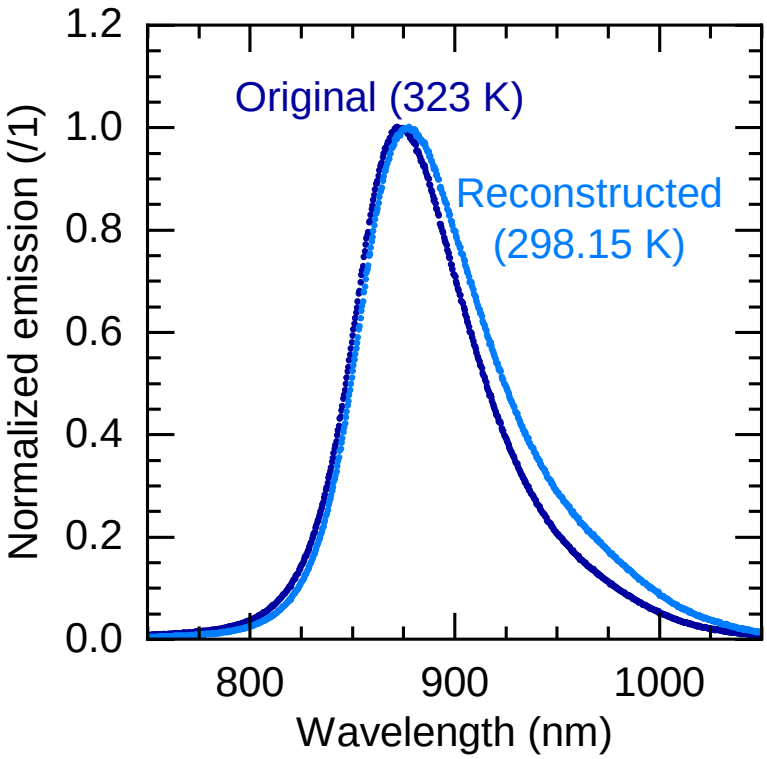

Supplementary Figure 6. Reconstruction of the emission spectrum at 298.15 K. The original PL spectrum is shown for comparison. The correction to a lower temperature increases the extent of sub-bandgap features and slightly shifts the PL peak to longer wavelengths.

Supplementary Table 1. Sensitivity of the calculation of $V_{oc,ideal}$ from the PL spectrum as a function of the error in the sample temperature extracted.

Assumed sample temperature during PL measurement	**280 K**	**300 K**	**323 K**	**340 K**	**360 K**
Calculated $V_{oc,ideal}$	1142.5 mV	1137.3 mV	1131.2 mV	1126.8 mV	1121.7 mV
Error on temperature	43 K	23 K	0 K	17 K	37 K
Error on $V_{oc,ideal}$	11.3 mV	6.1 mV	0 mV	4.4 mV	9.5 mV

Supplementary Methods 2 — Model for the relationship between *ERE* and minority-carrier lifetime τ

iV_{oc} can either be obtained from *ERE* and $V_{oc,ideal}$ (Equations (S5) and (S6)) or from the carrier concentrations (Equations (S10) and (S12)). Combining these two approaches in the general case (low or high doping) yields a relationship between *ERE* and τ:

$$iV_{oc} = V_{oc,ideal} - \frac{k_B T}{q}|\ln(ERE)| = \frac{k_B T}{q}\ln\left(\frac{n_e n_h}{n_i^2}\right), \tag{S14}$$

$$n_e = \frac{n_i^2}{N_A} + \Delta n \cong \Delta n = \Delta G\tau, \tag{S15a}$$

$$n_h = N_A + \Delta n = N_A + \Delta G\tau, \tag{S15b}$$

$$e^{\frac{qV_{oc,ideal}}{k_B T}} ERE = \frac{(N_A + \Delta G\tau)\Delta G\tau}{n_i^2}. \tag{S16}$$

Assuming a uniform excess carrier concentration, ΔG can be obtained from the short-circuit current density J_{sc} and the thickness L of the sample ($J_{sc} = qL\Delta G$). Rearranging Equation (S16) as a quadratic equation with $x = \Delta G\tau$ and solving it gives τ as a function of *ERE*:

$$\tau = \frac{qL}{2J_{sc}}\left(\sqrt{N_A^2 + 4n_i^2 e^{\frac{qV_{oc,ideal}}{k_B T}} ERE} - N_A\right). \tag{S17}$$

n_i is obtained from:

$$n_i = \sqrt{N_C N_V} e^{\frac{-E_g}{2k_B T}}, \tag{S18}$$

with N_C=8×10^{17} cm^{-3} and N_V=1.8×10^{19} cm^{-3} the effective densities of states in the conduction and valence bands, respectively,[8] and E_g the effective bandgap of the sample, taking into account sub-bandgap features. The assumptions for the input parameters (L, J_{sc}, N_A, E_g, n_i, and $V_{oc,ideal}$) for the shaded regions in Figure 2a can be found in Supplementary Table 2. The same J_{sc}, E_g, and n_i

values were used for the calculation of iV_{oc} from experimentally determined N_A, τ, and L presented in Figure 2b. These experimentally determined input parameters are tabulated in the associated Source Data File. Given that As doping increases sub-bandgap features—hence reducing the effective bandgap of the sample—different values were used for E_g, n_i, and $V_{oc,ideal}$ depending on whether the samples were Cu-doped or As-doped. It is important to note that other combinations of input parameters can yield similar regions in Figure 2a. For example, the red region can be obtained with a fixed N_A=8×10^{15} cm^{-3} and $V_{oc,ideal}$ varying between 1100 mV and 1120 mV. Without information on the actual acceptor concentration or the extent of sub-bandgap features, it is hard to tell whether the acceptor concentration is high or $V_{oc,ideal}$ is low.

Supplementary Table 2. Input parameters for the modeled relationship between ERE and τ for the shaded regions in Figure 2a and for the calculations of iV_{oc} from N_A and $\tau_{TRPL\text{-}tail}$ in Figure 2b. In the latter case, we use the actual absorber thickness *L*, reported in the associated Source Data File.

Input parameter	L (μm)	J_{sc} (mA.cm^{-2})	N_A (cm^{-3})	E_g (eV)	n_i (cm^{-3})	$V_{oc,ideal}$ (mV)
Blue region (Cu-doped)	5	30	2×10^{14}–2×10^{15}	1.42	3.8×10^{6}	1150
Orange region (As-doped)			8×10^{14}–8×10^{15}	1.39	6.8×10^{6}	1120
Red region (highly As-doped)			8×10^{15}–2×10^{16}			

Supplementary Methods 3 — Estimation of the minority-carrier lifetime from tail-fitting of the TRPL decay and validation of the technique

To estimate the minority-carrier lifetime in finished devices, we fit the tail of the TRPL decay with a single exponential to extract the TRPL-tail characteristic decay time $\tau_{TRPL\text{-}tail}$, as shown in Supplementary Figure 7 (dashed dark blue line). For this tail-fitting technique to be accurate, two assumptions must be verified: 1) the excess carrier concentration is approximately constant across the sample, and 2) net charge currents in and out of the absorber are negligible. In the tail of the TRPL decay, Assumption 1) is generally verified given that, long-enough after the laser excitation pulse, diffusion of charge carriers leads to homogeneous concentrations. On the other hand, Assumption 2) is not necessarily verified for finished devices with a junction at the front, where carrier separation can occur, leading to local charging and discharging of the contact layer.

As shown by Moseley *et al*., the characteristic decay time $\tau_{TRPL\text{-}tail}$ extracted from fitting the tail of the TRPL curve diverges from the actual minority-carrier lifetime τ when the band bending at the front of the device increases—that is, with increasing n-type doping of the front electron contact and increasing p-type doping of the absorber.[9] However, at low photon fluences, the mismatch between the actual minority-carrier lifetime and the characteristic decay time of the TRPL tail becomes substantial *only when* the band bending at the front of the device is high enough, with high doping of the electron contact layer or the absorber. In such cases, advanced modeling of the entire device is required to estimate the minority-carrier lifetime from fitting the full TRPL decay curve. When the doping is moderate in both the electron contact and the absorber—as is the case with our samples (the MZO electron contact is not intentionally doped

and $N_A < 5\times10^{15}$ cm^{-3} for all but a couple of our samples)—the TRPL-tail characteristic decay time $\tau_{TRPL\text{-}tail}$ remains close to the actual minority-carrier lifetime.

We demonstrate this in Supplementary Figure 7: the characteristic decay times $\tau_{TRPL\text{-}tail}$ we extract from fitting the tail of the TRPL match the actual minority-carrier lifetimes τ obtained from fitting the entire TRPL data using the COMSOL app developed by Moseley *et al.*.[10] The values match across 3 orders of magnitude—from a few nanoseconds to a few microseconds—with absorber acceptor concentrations N_A between 2×10^{14} cm^{-3} and 5×10^{15} cm^{-3}. As expected, this technique is less reliable at higher lifetimes and higher N_A, with $\tau_{TRPL\text{-}tail}$ becoming sensitive to the fitting range in Supplementary Figure 7d. However, because our MZO electron contact layer is not heavily doped, this effect is not as strong as reported by Moseley *et al.*.[9] As a result, in Supplementary Figure 7d, fitting the decay in different regions of the TRPL tail gives a range of decay times between 500 and 5000 ns, within a half order of magnitude of the actual minority-carrier lifetime τ = 1500 ns extracted from modeling. Thus, the mismatch between $\tau_{TRPL\text{-}tail}$ and τ remains below 70%, leading to a deviation in the calculation of iV_{oc} of $(k_BT/q)\ln(1.7) <$15 mV, in agreement with the results obtained in Figure 2b. As shown in Supplementary Figure 9, the deviation becomes more significant when $N_A > 3\times10^{15}$ cm^{-3}: the iV_{oc} calculated from the N_A–$\tau_{TRPL\text{-}tail}$ model then diverges from the iV_{oc} calculated from *ERE* measurements.

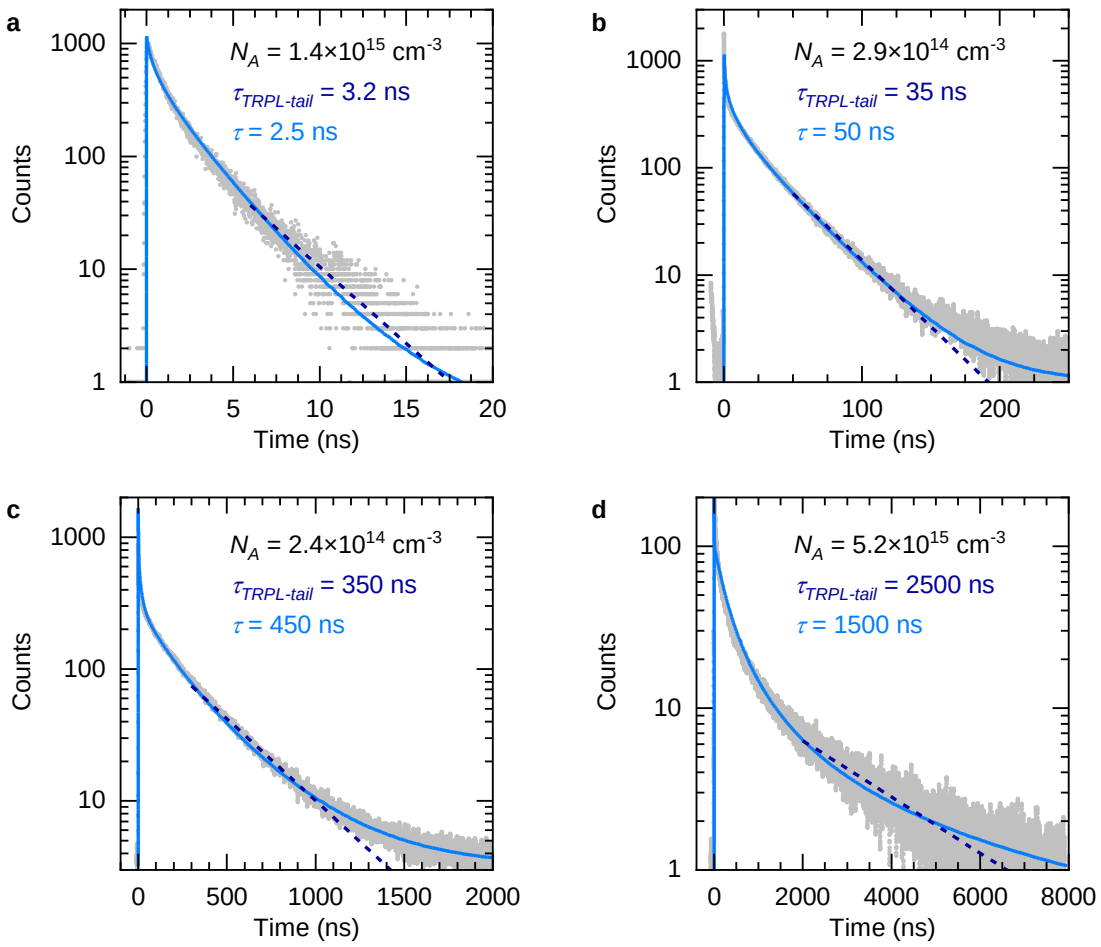

Supplementary Figure 7. Validation of the tail-fitting technique used to estimate minority-carrier lifetimes in finished devices from time-resolved photoluminescence (TRPL) decays. Experimental TRPL data (gray data points) along with modeled TRPL decays (full light blue lines) and local exponential fittings of the tail of the decay (dashed dark blue lines) are shown for devices with increasing minority-carrier lifetimes, from a few nanoseconds **(a)** to a few microseconds **(d)**, with acceptor concentrations N_A between 2×10^{14} cm^{-3} and 5×10^{15} cm^{-3}. The TRPL-tail characteristic decay time $\tau_{TRPL\text{-}tail}$ closely match the actual minority-carrier lifetime τ obtained from modeling the full TRPL decay using the COMSOL app from Moseley et al..[9,10] Full data for the TRPL decays reported in this study can be found in Supplementary Data 4.

Supplementary Table 3. $V_{oc,ideal}$, *ERE*, and iV_{oc} of the samples shown in Figure 1c. The samples are numbered from the lowest As-doped (sample #1) to the highest As-doped (sample #5). For each sample, $V_{oc,ideal}$ was calculated from the absorptance determined from the photoluminescence spectrum of a representative portion of the film, as detailed in Supplementary Methods 1, and the ±10 mV error represent the uncertainty associated with the measurement. *ERE* was measured on multiple locations across the samples (6 measurements per sample) to calculate iV_{oc} from $V_{oc,ideal}$, and the error on iV_{oc} represent the combined uncertainty from the calculation of $V_{oc,ideal}$ and from the standard deviation in the *ERE* measurement. The statistical source data for the *ERE* and iV_{oc} can be found in Supplementary Data 1.

Sample	Sample temperature during PL (K)	$V_{oc,ideal}$ (mV)	*ERE* (%)	iV_{oc} (mV)
#1	328	1100 ± 10	0.052	914 ± 11
#2	330	1086 ± 10	0.097	916 ± 13
#3	338	1072 ± 10	0.139	911 ± 13
#4	339	1063 ± 10	0.125	892 ± 11
#5	352	1049 ± 10	0.068	861 ± 11

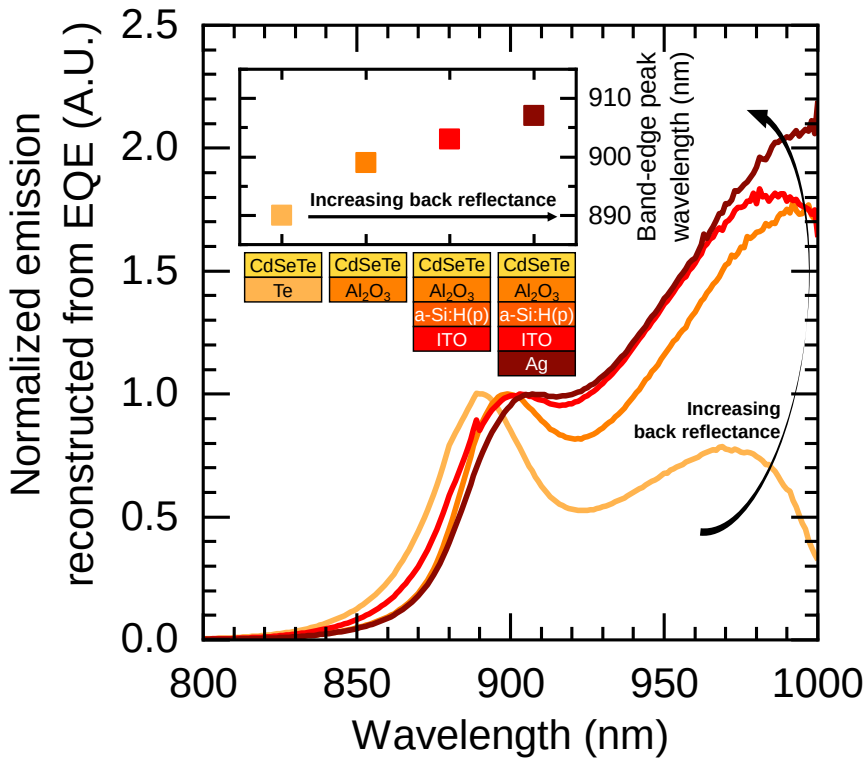

Supplementary Figure 8. Reproduction of Figure 1d on a standard wavelength scale. The wavelength of the band-edge PL peak, which increases with increasing reflectance, is shown in inset.

Supplementary Table 4. $V_{oc,ideal}$, ERE, and iV_{oc} of the samples shown in Figure 1d. Because the original EQE data is cut off at 1000 nm, portion of the $EQE \times \phi_{BB}$ spectrum is missing. As a result, the uncertainty is large (±20 mV) on the $V_{oc,ideal}$ calculations and, thus, on the iV_{oc} calculated from individual *ERE* measurements.

Back contact	$V_{oc,ideal}$ (mV)	ERE (%)	iV_{oc} (mV)
Te	1105 ± 20	0.16	940 ± 20
Al_2O_3	1083 ± 20	0.90	962 ± 20
Al_2O_3/a-Si:H(p)/ITO	1080 ± 20	1.57	973 ± 20
Al_2O_3/a-Si:H(p)/ITO/Ag	1072 ± 20	2.23	974 ± 20

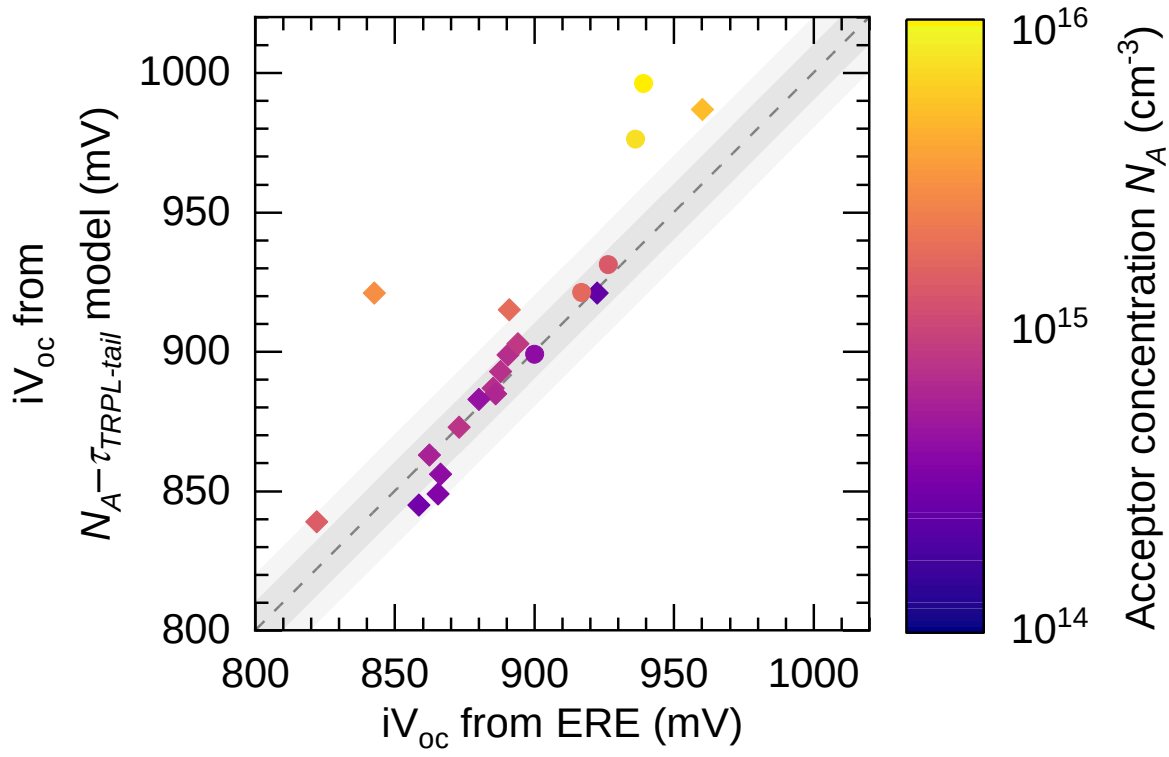

Supplementary Figure 9. Comparison between iV_{oc} calculated from *ERE* and iV_{oc} modeled from $\tau_{TRPL\text{-}tail}$ (from TRPL) and acceptor concentrations N_A (from C–V) including samples with N_A>3×10^{15} cm^{-3}. This Figure shows the same data as Figure 2b, this time including the high-acceptor-concentration outliers. The dashed line is the *y*=*x* equality line, the dark-grey and light-grey shaded regions correspond to the areas were the results match within ±10 mV and ±20 mV, respectively. Both approaches to calculate iV_{oc} agree when N_A<3×10^{15} cm^{-3} but diverge when N_A>3×10^{15} cm^{-3}, as tail-fitting of the TRPL decay gives an erroneous estimation of the minority-carrier lifetime at higher acceptor concentration, and extensive device modeling is then needed to accurately determine the minority-carrier lifetime (see Supplementary Methods 3 for details).[9,11] The input parameters for the N_A–$\tau_{TRPL\text{-}tail}$ model and for the calculation of iV_{oc} from *ERE* can be found in Supplementary Data 2. Full data for the TRPL decays and the C–V profiles of the devices reported here can be found in Supplementary Data 4 and Supplementary Data 5, respectively.

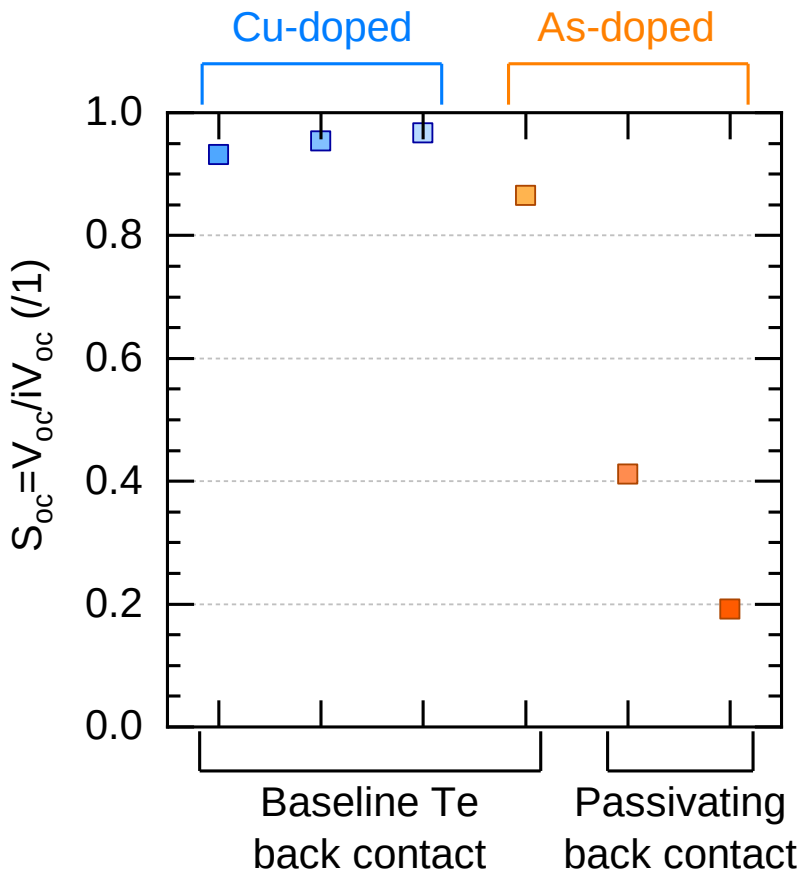

Supplementary Figure 10. Selectivity metric $S_{oc}=V_{oc}/iV_{oc}$ for the 6 characteristic samples presented in Figure 3. The color shade qualitatively indicates the sample selectivity ($S_{oc}=V_{oc}/iV_{oc}$), from lower selectivity samples (darker shade) to higher selectivity samples (lighter shade). All the samples with a Te back contact present a decent selectivity (S_{oc}>0.85)—in particular the Cu-doped samples (S_{oc}>0.93)—but the samples with a passivating back contact present a poor selectivity (S_{oc}<0.5), meaning that one of the contacts (we suspect the Al_2O_3/a-Si:H(p) one) preferrably extracts the "wrong" type of carriers (electrons in the case of the back hole contact). That is, the passivating back contact appears to be highly resistive to both electrons and holes—hence the excellent surface passivation and the high *ERE* and iV_{oc}—but more so to electrons—hence the low selectivity S_{oc}<0.5.

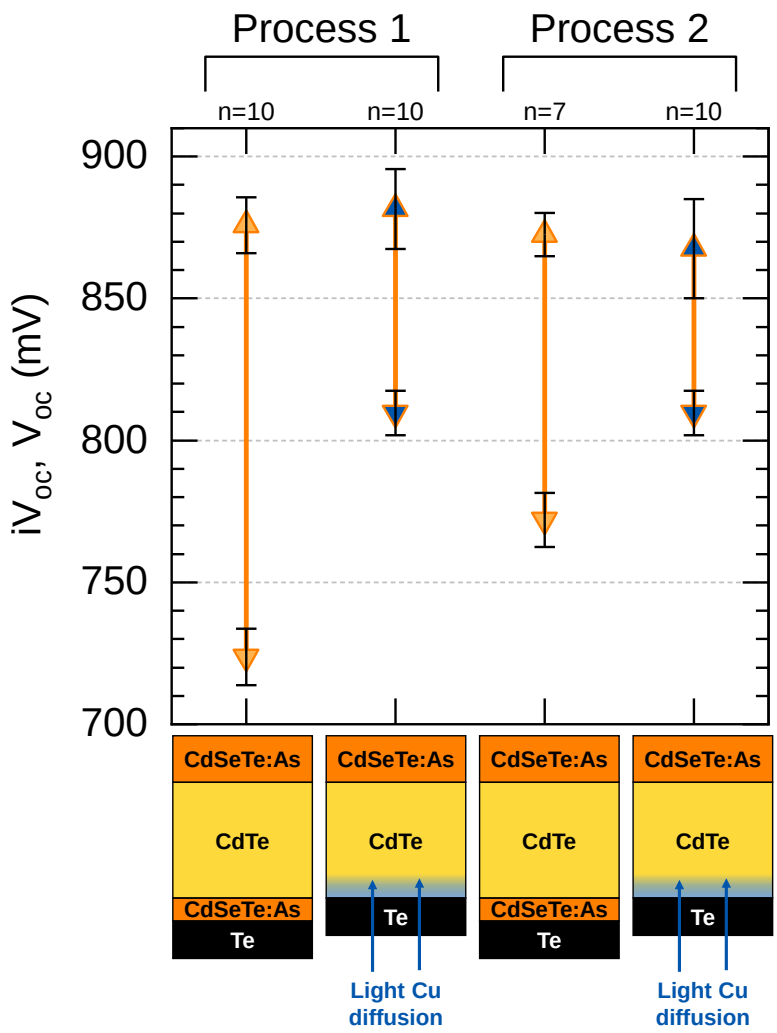

Supplementary Figure 11. Comparison between iV_{oc} and V_{oc} for samples fabricated with an identical As-doped front absorber and either a CdSeTe:As/Te or a CdTe:Cu/Te back interface. Each sample comprises n=7 to 10 devices, the exact number of which is indicated at the top of the graph. V_{oc} was measured on each device individually, and the error bars represent the standard deviation of the mean. For each sample, $V_{oc,ideal}$ was determined from the EQE of a representative device. *ERE* was measured on a representative portion of the devices (6 to 7, depending on the sample) to calculate iV_{oc} from $V_{oc,ideal}$, and the error bars on iV_{oc} represent the combined uncertainty from the calculation of $V_{oc,ideal}$ and from the standard deviation in the *ERE* measurement. The statistical source data can be found in Supplementary Data 3. The front absorber

consists of 500 nm of CdSeTe doped in-situ with As followed by 2600 nm of intrinsic CdTe. Different layers were used at the interface with the Te back contact: we either used another thin (200 nm) layer of As-doped CdSeTe, yielding a CdSeTe:As/Te interface; or we only performed a light CuCl treatment (no second CdSeTe layer) in order to achieve a shallow Cu diffusion at the back of the device, yielding a CdTe:Cu/Te interface. The duration of the post-deposition, post-$CdCl_2$-treatment high-temperature (1200 °C) anneal step is the only difference between the samples labeled “Process 1” and “Process 2”. The samples with a CdTe:Cu/Te interface exhibit a much better selectivity without any significant degradation of the passivation: the iV_{oc} is similar between all devices but V_{oc} improves appreciably for the Cu-treated samples. It is unclear at this point whether the wider bandgap of CdTe or the graded Cu doping profile are responsible for the improved selectivity.

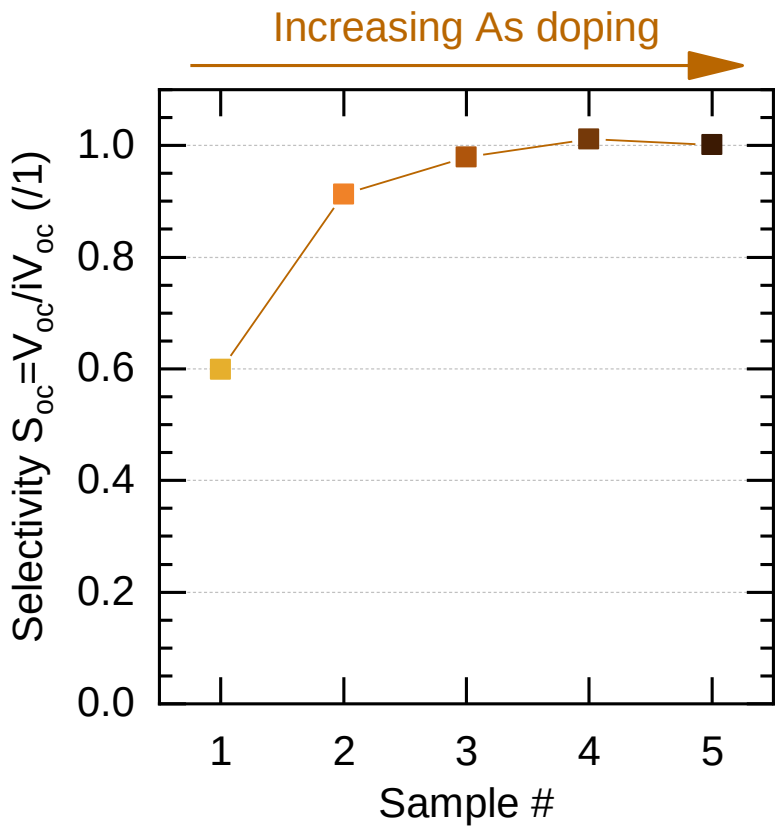

Supplementary Figure 12. Selectivity metric $S_{oc}=V_{oc}/iV_{oc}$ for the samples fabricated by First Solar presented in Figure 4. The selectivity of devices fabricated at First Solar improves with As doping, as the conductivity to holes is increased wheareas the conductivity to electrons is decreased at the back of the absorber. For each metric, the line is a guide to the eye.

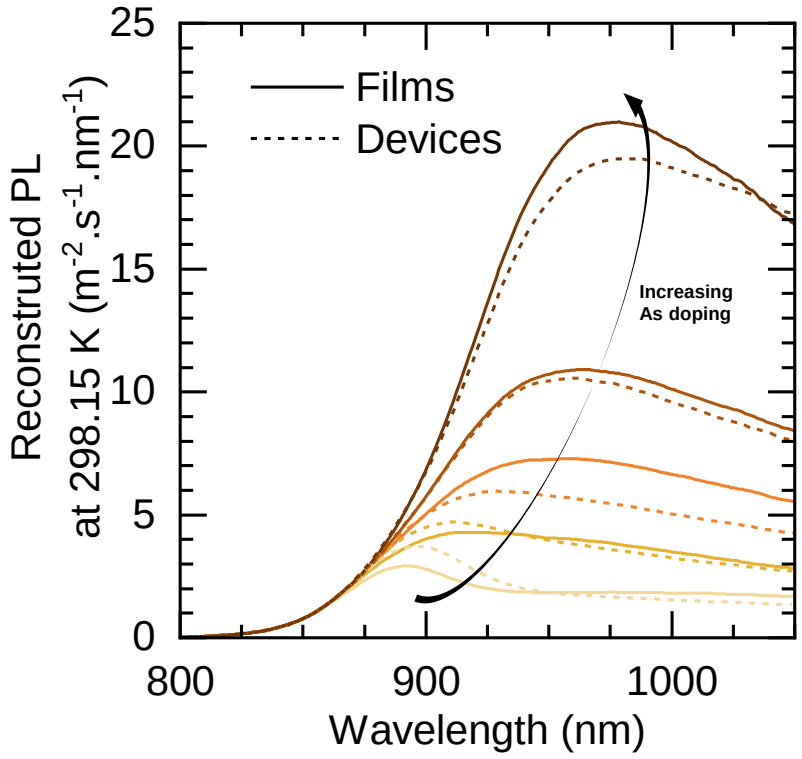

Supplementary Figure 13. Comparison between the temperature-corrected PL spectra from the films with a free back surface (also shown in Figure 1c) and from the finished devices fabricated by First Solar. For each level of As doping, the finished devices and the uncontacted films were fabricated together. As expected, each set exhibits similar sub-bandgap features. Consequently, these devices exhibit similar $V_{oc,ideal}$ values, as reported in Supplementary Tables 3 and 5.

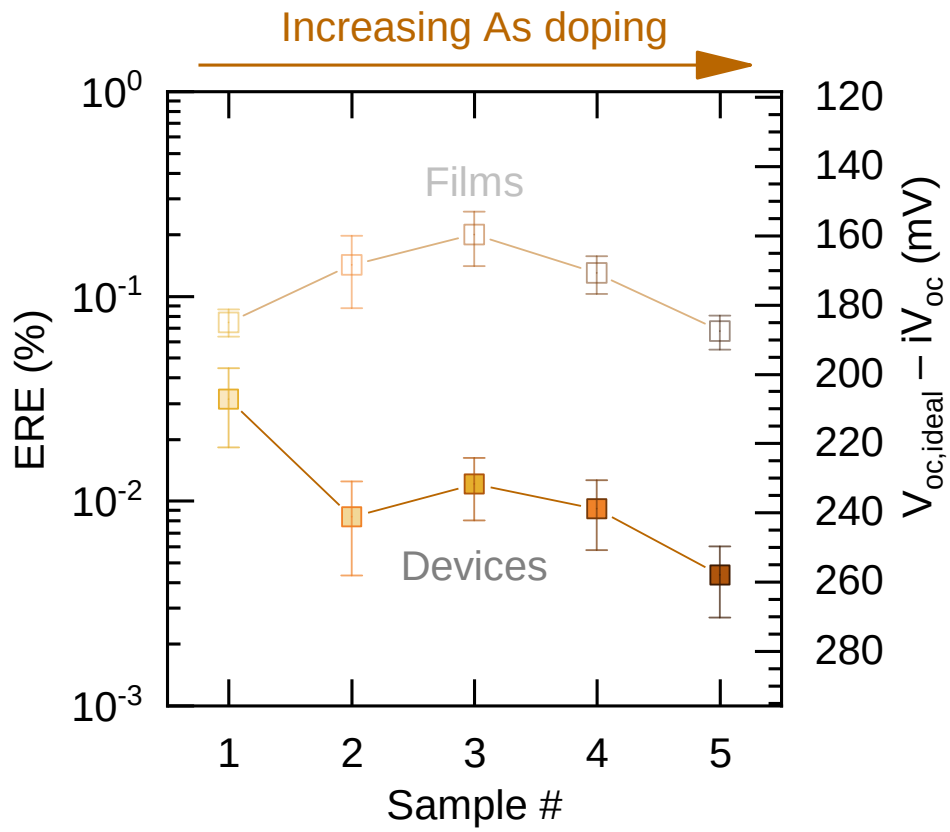

Supplementary Figure 14. Comparison between the *ERE* of the films with a free back surface (also shown in inset in Figure 1c) and from the finished devices fabricated by First Solar. For each level of As doping, the finished devices and the uncontacted films were fabricated together. On device samples, 17 *ERE* measurements were taken across each sample, and the error bars represent the standard deviation of the mean; on film samples, 6 *ERE* measurements were taken across each sample, and the error bars represent the standard deviation of the mean. The statistical source data can be found in Supplementary Data 1. For each metric, the line is a guide to the eye.

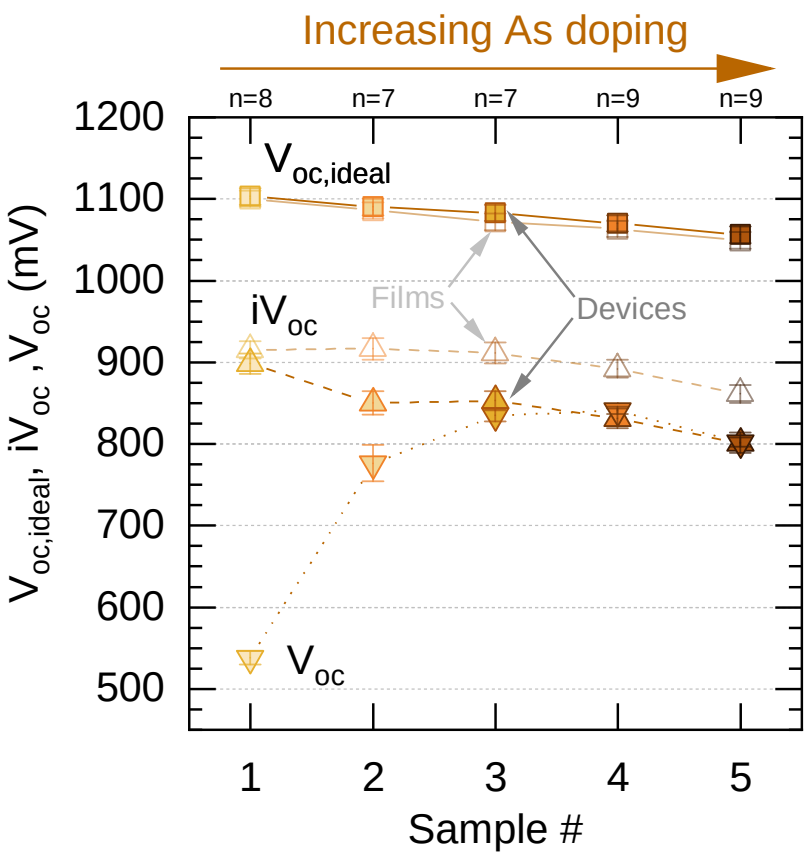

Supplementary Figure 15. Voltage loss analysis for the finished devices (also shown in Figure 4) and for the films with a free back surface fabricated by First Solar. For each level of As doping, the finished devices and the uncontacted films were fabricated together. On device samples, V_{oc} was measured on n=7 to 9 devices per sample, as indicated at the top of the graph, and the error bars represent the standard deviation of the mean. For each sample (devices and films), $V_{oc,ideal}$ was calculated from the absorptance determined from the photoluminescence spectrum of a representative portion of the sample, as detailed in Supplementary Methods 1, and the error bars represent the uncertainty associated with the measurement. *ERE* was measured on multiple locations across the samples (17 measurements per device sample, 6 measurements per film sample) to calculate iV_{oc} from $V_{oc,ideal}$, and the error bars on iV_{oc} represent the combined uncertainty from the calculation of $V_{oc,ideal}$ and from the standard deviation in the *ERE*

measurement. The statistical source data can be found in Supplementary Data 1. For each metric, the line is a guide to the eye. The effect of sub-bandgap features on the final V_{oc} is visible, in particular when comparing devices from Samples #4 and #5, for which V_{oc}=iV_{oc}. Indeed, V_{oc}=iV_{oc} is on average 30–40 mV higher for Sample #4 despite a ratio of *ERE* of only about 2.5—translating into a V_{oc} loss due to non-radiative recombination only about 20 mV higher for Sample #5. That is, the difference in sub-bandgap features between Sample #4 and #5 is responsible for the remaining 10–20 mV difference in V_{oc}, matching the difference in $V_{oc,ideal}$ (approximately 14 mV) between the samples. In other words, the difference in sub-bandgap features is responsible for about 30–50% of the voltage difference between Samples #4 and #5, non-radiative recombination being responsible for the remainder.

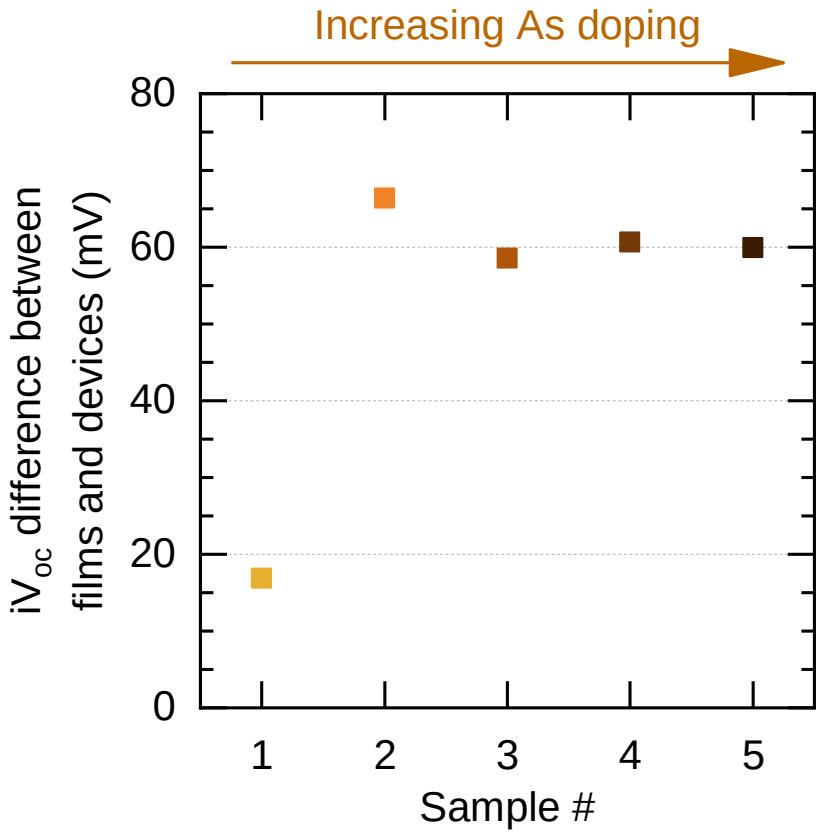

Supplementary Figure 16. iV_{oc} difference between films with a free back surface (no back contact) and finished devices fabricated by First Solar. For each level of As doping, the finished devices and the uncontacted films were fabricated together.

Supplementary Table 5. $V_{oc,ideal}$, ERE, iV_{oc}, V_{oc}, and S_{oc} of the samples shown in Figure 4. The samples are numbered from the lowest As-doped (sample #1) to the highest As-doped (sample #5). For each sample, $V_{oc,ideal}$ was calculated from the absorptance determined from the photoluminescence spectrum of a representative device, as detailed in Supplementary Methods 1, and the ±10 mV error represent the uncertainty associated with the measurement. *ERE* was measured on multiple devices across the samples (17 measurements per sample) to calculate iV_{oc} from $V_{oc,ideal}$, and the error bars on iV_{oc} represent the combined uncertainty from the calculation of $V_{oc,ideal}$ and from the standard deviation in the *ERE* measurement. V_{oc} was measured on n=7 to 9 devices per sample, as indicated in Figure 4, and the error bars represent the standard deviation of the mean. The statistical source data can be found in Supplementary Data 1.

Sample	$V_{oc,ideal}$ (mV)	ERE (%)	iV_{oc} (mV)	V_{oc} (mV)	S_{oc} (/1)
#1	1103 ± 10	0.031	898 ± 13	538 ± 8	0.60
#2	1090 ± 10	0.008	850 ± 14	776 ± 22	0.91
#3	1083 ± 10	0.012	853 ± 12	835 ± 7	0.98
#4	1070 ± 10	0.009	831 ± 12	841 ± 5	1.00
#5	1056 ± 10	0.004	801 ± 13	802 ± 6	1.00

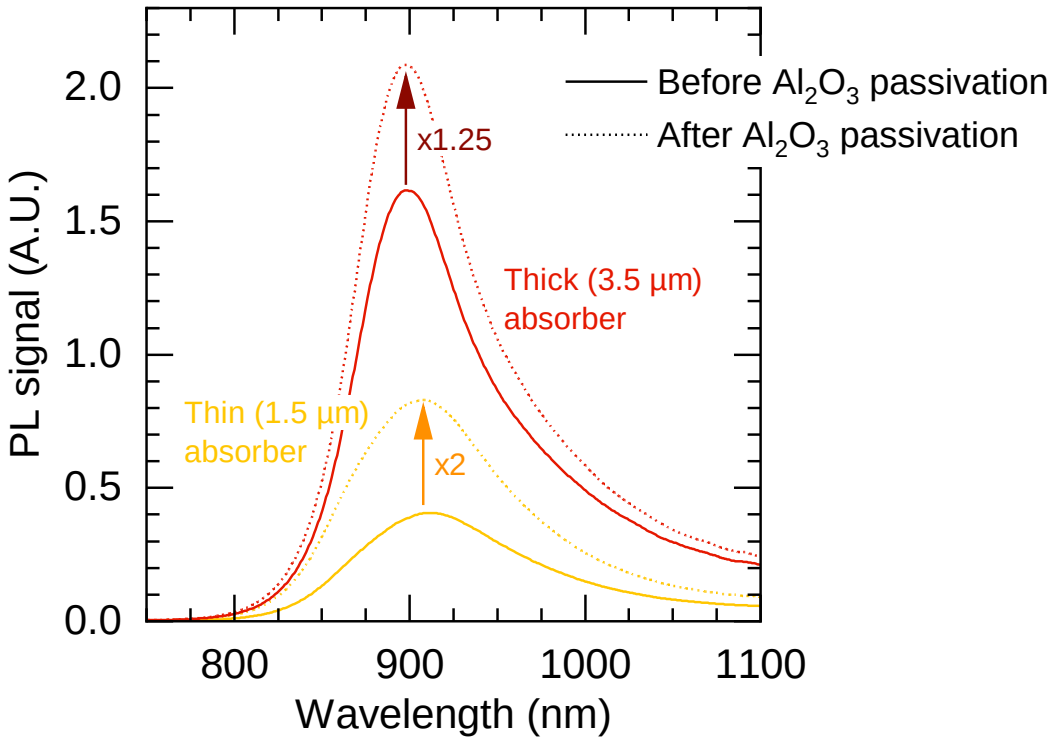

Supplementary Figure 17. Photoluminescence comparison before and after Al_2O_3 passivation on First Solar's samples with an (initial) free back surface. To better show the effect of modifying this back interface, samples with thin (1.5 µm) and thick (3.5 µm) absorbers were used. The change in magnitude of the integrated PL is shown with arrows. The increase in PL upon addition of an Al_2O_3 passivation layer is moderate (< 2×), with the expected stronger effect when modifying the back interface in the case of a thinner absorber. This suggests that other sources of recombination limit the luminescence and, thus, the iV_{oc} of these samples. Corresponding PL values measured on the film (back) side of the samples before and after Al_2O_3 processing show a 10 times improvement in intensity with Al_2O_3, demonstrating the improvement in the passivation of the back interface. Data reproduced from Grover, no permission required.[12]

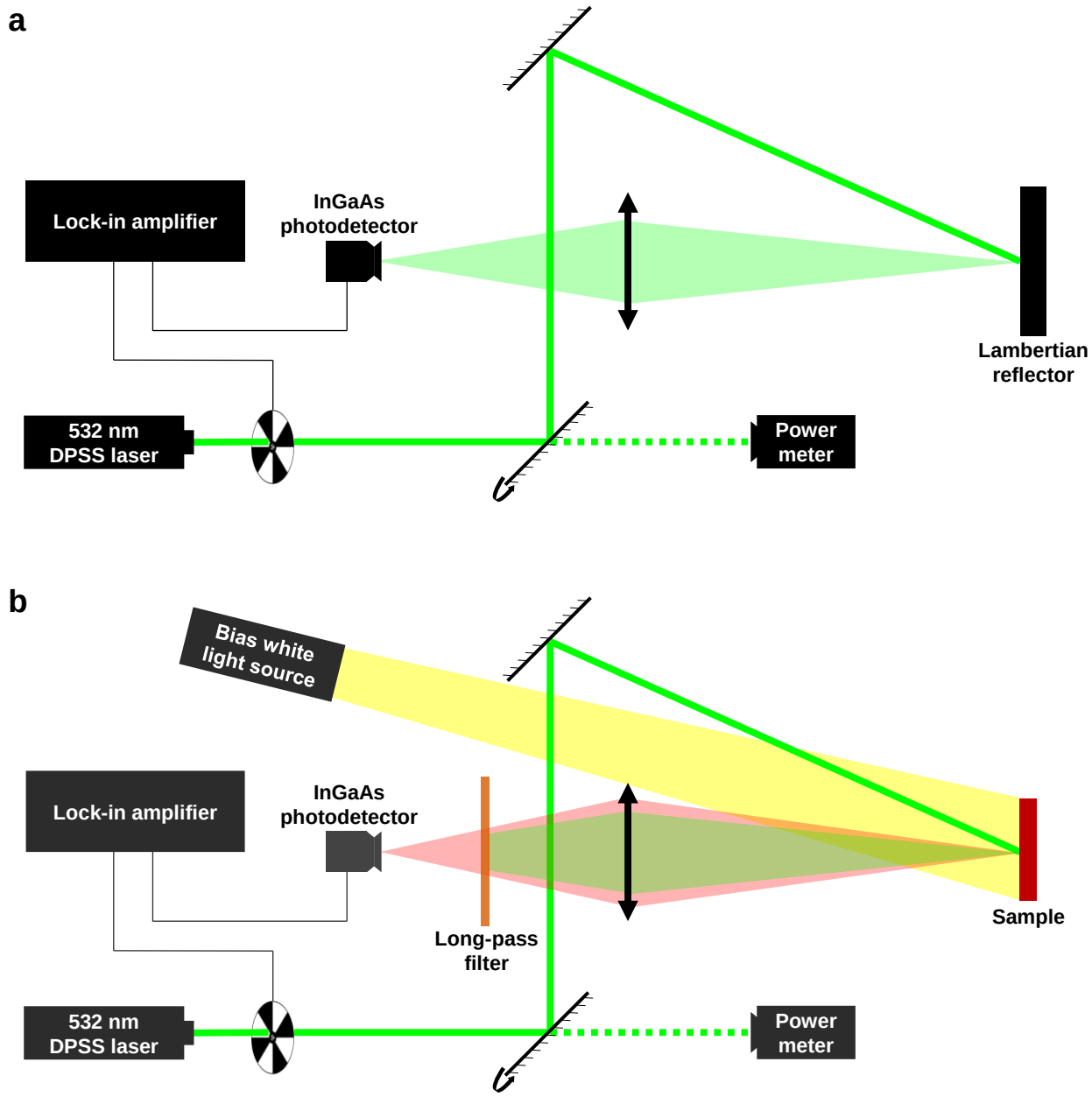

Supplementary Figure 18. Schematic of the ERE tool used in this study. a) Tool configuration during calibration of the incoming laser photon current. **b)** Tool configuration during sample measurement. The bias white LED light source is set to a 1-sun-equivalent photon current density.

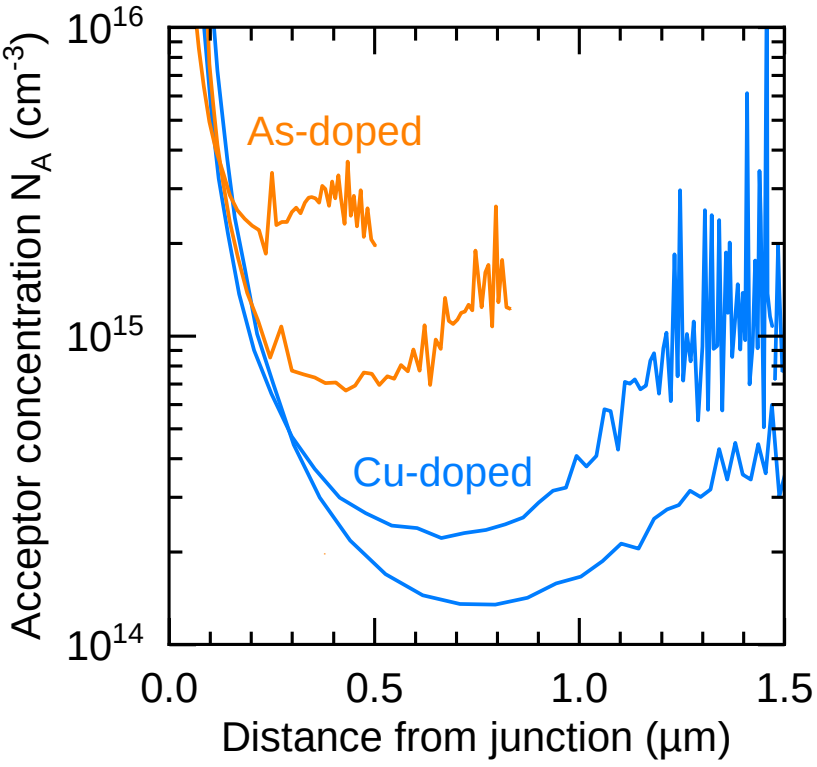

Supplementary Figure 19. C–V measurement results. Carrier concentration versus distance from junction extracted from C–V measurements on representative As-doped and Cu-doped devices.[13] In line with previous reports, the acceptor concentration is typically an order of magnitude higher with As doping.[14,15] Full data for the C–V profiles of the devices reported in Figure 2b and Supplementary Figure 9 can be found in Supplementary Data 5.

Supplementary References

1 Ross, R. T. Some Thermodynamics of Photochemical Systems. *J. Chem. Phys.* **46**, 4590-4593, doi:10.1063/1.1840606 (1967).

2 Würfel, P. The chemical potential of radiation. *J. Phys. C* **15**, 3967-3985, doi:10.1088/0022-3719/15/18/012 (1982).

3 Vandewal, K., Tvingstedt, K., Gadisa, A., Inganas, O. & Manca, J. V. On the origin of the open-circuit voltage of polymer-fullerene solar cells. *Nat. Mater.* **8**, 904-909, doi:10.1038/nmat2548 (2009).

4 Rey, G. *et al.* Absorption Coefficient of a Semiconductor Thin Film from Photoluminescence. *Phys. Rev. Appl.* **9**, doi:10.1103/PhysRevApplied.9.064008 (2018).

5 Ganapati, V., Steiner, M. A. & Yablonovitch, E. The Voltage Boost Enabled by Luminescence Extraction in Solar Cells. *IEEE J. Photovolt.* **6**, 801-809, doi:10.1109/jphotov.2016.2547580 (2016).

6 Würfel, U., Cuevas, A. & Würfel, P. Charge Carrier Separation in Solar Cells. *IEEE J. Photovolt.* **5**, 461-469, doi:10.1109/JPHOTOV.2014.2363550 (2015).

7 Onno, A., Chen, C., Koswatta, P., Boccard, M. & Holman, Z. C. Passivation, conductivity, and selectivity in solar cell contacts: Concepts and simulations based on a unified partial-resistances framework. *J. Appl. Phys.* **126**, 183103, doi:10.1063/1.5117201 (2019).

8 Gloeckler, M., Fahrenbruch, A. L. & Sites, J. R. in *3rd World Conference on Photovoltaic Energy Conversion (WCPEC).* 491-494.

9 Moseley, J., Krasikov, D., Lee, C. & Kuciauskas, D. Diverse simulations of time-resolved photoluminescence in thin-film solar cells: A SnO2/CdSeyTe1−y case study. *J. Appl. Phys.* **130**, doi:10.1063/5.0063028 (2021).

10 Moseley, J., Krasikov, D. & Kuciauskas, D. in *48th IEEE Photovoltaic Specialists Conference.* 1687-1690.

11 Jundt, P., Kuciauskas, D. & Sites, J. in *47th IEEE Photovoltaic Specialists Conference.* 1408-1412.

12 Grover, S. in *4th CdTe workshop* (2020).

13 Hegedus, S. S. & Shafarman, W. N. Thin-film solar cells: device measurements and analysis. *Prog. Photovolt. Res. Appl.* **12**, 155-176, doi:10.1002/pip.518 (2004).

14 Metzger, W. K. *et al.* Exceeding 20% efficiency with in situ group V doping in polycrystalline CdTe solar cells. *Nat. Energy* **4**, 837-845, doi:10.1038/s41560-019-0446-7 (2019).

15 Munshi, A. H. *et al.* in *47th IEEE Photovoltaic Specialists Conference.* 1824-1828.